

Design, fabrication and characterisation of Si nanopillars-based photonic crystal for mechanical sensing

Author: Elena López Aymerich

Supervisor: Albert Romano-Rodríguez, MIND-UB Physics Faculty Dept. of Electronic and Biomedical
Engineering

Abstract—In this work the first results of the experimental implementation of silicon nanopillars hexagonal arrays acting as photonic crystals with the aim of their use as force sensors are presented. The starting point are two previous bachelor and master thesis that have shown the theoretical potentialities of such a structure acting as a photonic crystal and as a mechanical sensor due to deflection of the nanopillars. Here we present the optimization of the fabrication procedure of these nanostructures, based on a sequence of complex processes carried out in Clean-Room environment, and the support of simulations and morphological analysis via Scanning Electron Microscopy and the results obtained from Fourier Transform Infra-Red spectroscopy characterisation match the simulations of the photonic crystal, with bandgaps in the near infrared range, and pave the way in the use of such structures for mechanical testing in biomedical applications.

Index Terms— Nanophotonics: infra-red, nanopillars, photonic crystal, silicon.

I. INTRODUCTION

THE nature observation has been for humans a source of inspiration to imitate in order to improve in different ways electronic and optic devices. One good example is the case of photonic crystal structures, which are found in nature in opal minerals or butterfly wings and are imitated nowadays in several optical systems. Photonic crystals are defined as periodic arrangements of dielectric nanostructures inside a dielectric environment, both with quite different refraction indexes. Depending on the number of directions in which this period arrangement occurs, we would distinguish between one, two or three dimensional photonic crystals. Photons in a photonic crystal behave analogously as electrons do in a solid-ionic crystal. If the dielectrics forming the photonic crystal structure strongly differ in their refraction indexes and if these materials show low light absorption, reflections and refractions would be promoted at the interfaces between them and propagation of only certain wavelengths will occur. Those which are allowed by the structure are called light modes, those which are not, are called forbidden modes. Tuning the photonic crystal geometry design in the proper way a control over these permitted and non-permitted propagation wavelengths allows the appearance of photonic bandgaps, a

set of frequencies at which photons are forbidden to propagate in the crystal structure and, thus, produce their complete absorption. We would define a complete photonic band gap as the frequency range at which photon propagation in any direction in the crystal is forbidden [1].

One possible application of photonic crystals would be their use as mechanical sensors. Since the allowed bands of electromagnetic wave propagation are strongly correlated to the geometry of the crystal itself, we would expect that a mechanical induced change in the nanostructured arrangement, a deformation, would produce a change in the photonic band gap position and/or or width.

This system has been conceived for the study of the biological models based on mechanical stresses during growth and regeneration of tissues and, hence, would allow to evaluate the stopping mechanisms of this growth and to investigate, for example, whether cancer cells suffer less stresses than sane cells [2]. This application, thus, limits our photonic crystal design in several ways. First of all, the use of a biocompatible material and the construction of a photonic crystal large enough to sustain the tissue are necessary. On the other hand, and in relation to the optical properties, the material should have a refraction index larger than water based solutions (whose value is around 1.33) used for maintaining the cells alive during the sensing processes, as the system should be designed to perform in-vivo studies. Moreover, the

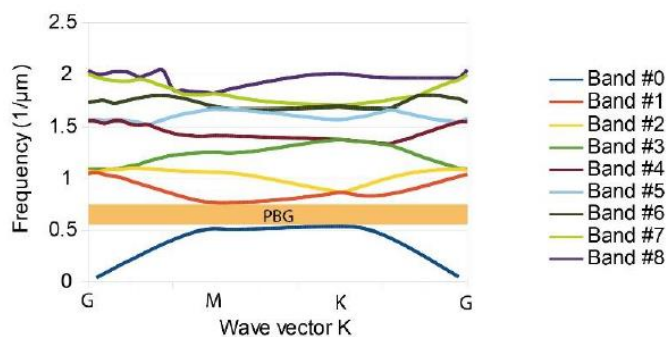


Fig. 1. Energy bands structure for a photonic crystal based on silicon nanopillars of 3 μm length and 100 nm radius, arranged in a hexagonal lattice with a pitch of 500 nm. The full photonic bandgap here observed is centered around 1.5 μm wavenumbers. Taken from [2].

photonic bandgap would be placed in an electromagnetic range where the biological samples show low absorption in order not to disturb the light propagation. This means that we would need to place our photonic crystal bandgap in the range of Near Infra-Red (NIR) wavelengths.

The aim of this work is to put in practice the results obtained in previous works carried out in our group that showed the potential capability of photonic crystals based on hexagonal arrays of silicon nanopillars to act as mechanical sensors for the first time.

In order to design the photonic crystal, a starting point has been the TFG of J. Esteve [3]. With the help of simulations the optimal periodic arrangement, the nanopillars radii and the separation between them (pitch) of the photonic crystal where the band gap in IR wavelength range were searched for. The software used during this first approach was *OptiFDTD 32-bits* (<http://optiwave.com/>). One of the first conclusions of that work had been that a suitable material needed to be used could be silicon, whose refraction index value is 3.42, which would correspond to the high refraction index material. In addition, silicon technology is widely known and advanced enough for the implementation and development of the fabrication process. However, we have not found previous results of using these tools for the fabrication of a set of structures as large (up to 3 μm) as the ones envisaged here. Photonic band gap calculations in the desired range and TE and TM electromagnetic modes evaluated in different crystallographic arrangements with horizontal light incidence, perpendicular to the nanopillars' length, showed that hexagonal distribution of the nanopillars gives rise to a photonic band gap in the Near-Infrared range of the electromagnetic spectrum, what matches the requirement about the light operation range of the structure. Further 2D simulations had been carried out with *COMSOL Multiphysics 5.0* (<https://www.comsol.com>). They have shown that a full photonic band gap of an hexagonal nanopillar arrangement with pitch and radius values of 500 nm and 100 nm, respectively, is found around 1.5 μm [2]. The energy bands of the photonic crystal and its different light modes are shown in Fig. 1.

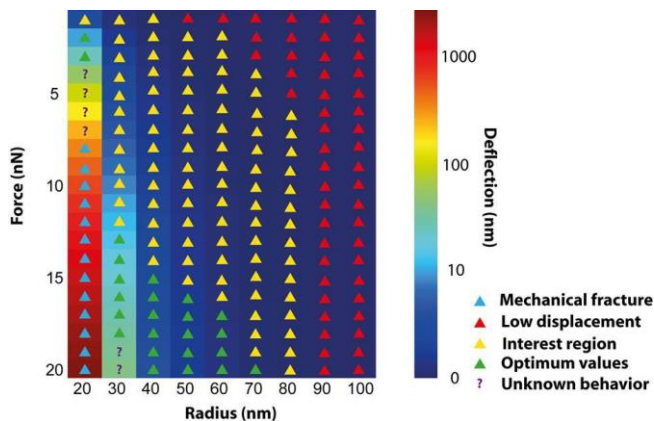


Fig. 2. Color map showing the simulated deformation of cylindrical silicon pillars with constant length of 3 μm . The axis show the force applied and pillars radius simulated. Taken from [2].

Focusing in another direction, the deflection capability of the nanostructure arrangement was also simulated and verified because of the mechanical stress sensing goal of our structure. The results obtained from these simulations are shown in Fig. 2 where it can be observed that the deflection is higher in pillars with smaller radii.

However, there is still no study showing that the deflection of the pillars due to mechanical stress, can give any detectable change in the photonic crystal light modes and forbidden modes.

II. FABRICATION

The fabrication of the structures has been performed using a lithographic process employing electron beam lithography (EBL) [4], followed by a lift-off process and the final nanopillars were obtained via chemical reactive plasma etching.

First of all, and in order to determine the optimal exposure conditions, different nanopillars' arrays have been defined with a total of 13 different electron beam dose conditions separated one from the next by a 20% factor, starting at 250 $\mu\text{C}/\text{cm}^2$ to 870 $\mu\text{C}/\text{cm}^2$ and for structures combining 5 different radii (20 - 100 nm) and 3 different pitches (300 - 500 nm).

The process starts with the photoresist deposition. The resist used is the CSAR-P-6200-9 resist which is a positive-tone electron-beam photoresist. It is spin-coated at 5200 rpm for 1 min, giving rise to a nominal thickness of 180 nm. A post bake at 180 $^{\circ}\text{C}$ for 3 min is performed in order to evaporate the remaining solvents and harden the photoresist layer.

After this spin coating step, an EBL process is performed to irradiate the photoresist. A Jeol JEB-9500 device is used, operating at 100 kV and with a resolution down to 10 nm. Because EBL can-not work with circular patterns, the system software approaches these curved geometries with regular polygons with a large number of edges what leads to a large time consuming exposure. Hence, the pattern finally used is a composed-figure with a rectangle in the centre and 4 trapezia that, together, mimic a circular-like shape, as shown in Fig. 3c. Moreover, the total written area is a 1x1 mm^2 , since this is the maximum area that the system allows to write without moving the substrate, we are interested in reduction of the total process time and minimising stitching errors, as larger areas would require optical alignment between the writing fields. The EBL dose used during the exposition goes from 250 $\mu\text{C}/\text{cm}^2$ in the case of nanopillars of radius 100 nm to 770 $\mu\text{C}/\text{cm}^2$, for radius of 20 nm. Finally, development of the resist is performed for 1 min and using AR-P645 developer in order to remove the electron irradiated photoresist, followed by isopropanol rinsing.

Following the EBL process lift-off metallization is performed. The first step is to deposit the metallic layer (aluminium in our case) on top of the EBL patterned substrate. During this process, an electron beam evaporation system operating at a deposition rate of 4 nm/s and a final thickness of 20 nm is used. A slow deposition rate is used in order to

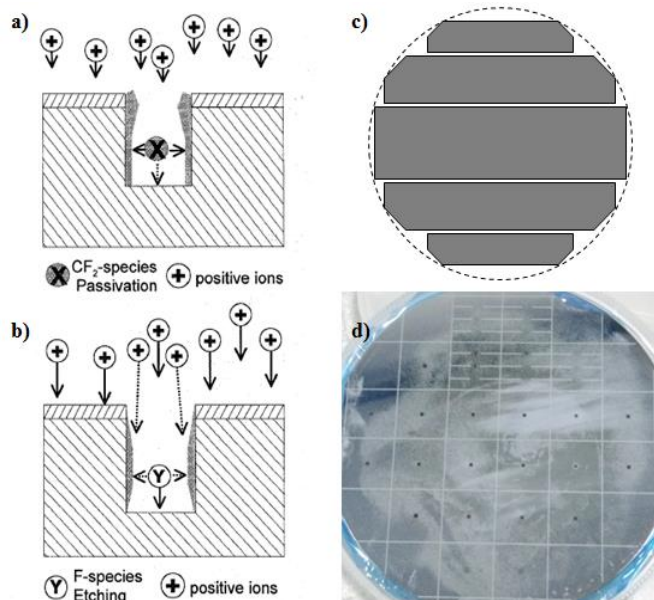


Fig. 3. Bosch process scheme divided in (a) the first delivery of SF_6 and (b) the following delivery of C_4F_8 [5]; (c) circular-like figure used as pattern for the EBL process; (d) top view of one of the resulting wafers.

minimize the substrate heating during the aluminium bombardment, since the photoresist is temperature sensitive. The lift-off process is carried out by submerging and sonicating the wafer in AR-P-770 solution, photoresist remover, for 5 -10 min, followed by isopropanol rinsing.

Finally, the nanopillars fabrication is carried out using chemical reactive ion etching. The approach uses the introduction of two gases into the chamber, which are sulphur fluorine (SF_6) and octafluorocyclobutane (C_4F_8), giving rise to the etching process and to the walls protection or passivation, respectively. This can be performed either via a Bosch or a pseudo-Bosch process, both schematically represented in Figs. 3a and 3b. The main differences between both is the fact that with the Bosch process the etching is carried out using alternate pulses of SF_6 and C_4F_8 , leading to high etching rates but less vertical walls are obtained, while the pseudo-Bosch process uses a mixture of both gases, giving rise to a slower process but more vertical walls are etched. This difference clearly affects the final geometry of the nanopillars.

During these months, up to four consecutive generations of samples have been fabricated, with the aim of optimizing the fabrication process and device geometry, where the last generation's devices showed the best geometries. These samples consist on a fabricated area of $1 \times 1 \text{ mm}^2$ that contains a $660 \times 660 \mu\text{m}^2$ nanopillars zone enclosed by a $20\mu\text{m}$ -wide wall and with 4 square-shaped grating structures, attached to the centre of each wall side, of $150 \times 150 \mu\text{m}^2$ and with a periodicity of $1 \mu\text{m}$. The purpose of these grating structures is to allow the light to be coupled to the photonic crystal using a source of light introduced by an optical fiber and to extract the light after passing through the structure.

It is important to point out that not only photonic crystal

structures have been developed, but also structures specifically designed to perform atomic force microscopy (AFM) characterisation to analyse their mechanical properties. They consist on rectangular arrays of equidistant pillars of different radii but are not used in this work. Fig. 3d shows a 10-cm in diameter silicon wafer after the whole fabrication process and diced already into $1.5 \times 1.5 \text{ cm}^2$. The 5 diced squares at the top that show 6 horizontal lines in it, correspond to the areas where the nanopillars for AFM study are located.

III. SIMULATION

Parallel to the fabrication process, simulations have been carried out in order to solve experimental challenges that previous simulations did not take into account.

The first and very important change compared to previous works is the configuration of the light incidence in the photonic crystal. Because the sample is bulk silicon, horizontal incidence would result in strong dispersions of light in the bulk, so that little light would arrive to the exiting grating. For this, a spectroscopic set up was used, which imposed a vertical incidence of light which was not considered in the previous simulations afore before where, in order to perform the mechanical sensor measurements, light introduction was perpendicular to the pillars length. A direct consequence of this change is the fact that now the height of nanopillars plays an important role and, thus, simulations for different heights have also been performed. Finally, since scanning electron microscope (SEM) analysis has shown tapering of the pillars radius (further discussed in the SEM subsection in the analysis part), simulations for pillars with different radii have been carried out.

In order to perform straightforwardly these simulations, *Lumerical FDTD* (Finite Difference Time-Domain) software (<https://www.lumerical.com/>) instead of Optiwave FDTD has been used, since it allows 3D structures to be simulated. This

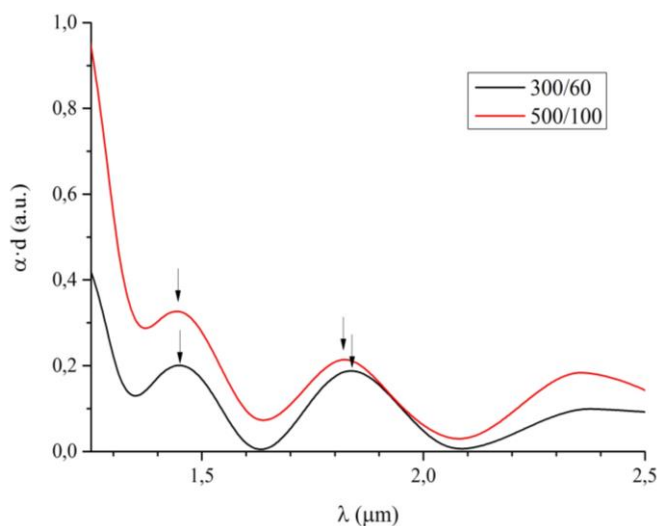


Fig. 4. Representation of the simulated absorbance as a function of the wavelength for structures with pitch 300 nm and radii 60 nm (black) and pitch 500 nm and radii 100 nm (red).

TABLE I
SIMULATION RESULTS

Sample	Peak 1 (μm)	Peak 2 (μm)
500/100	1.44	1.82
300/60	1.45	1.84

Absorption peak wavelengths obtained from the simulations. The notation used for the sample, name is pitch/radii, both in nm.

algorithm is specialized in the study of propagation of electromagnetic waves in different materials, structures and dimensions.

Since the photonic crystal behaviour can be approached to a solid-ionic crystal, and in order to simplify the simulations set and run, a single hexagonal Bravais cell has been simulated. The use of the right periodic boundary conditions allows us to consider having an infinite 3D hexagonal crystal and to understand the results as the electromagnetic waves interaction with this kind of system.

The results obtained show that a zone where maxima and minima of light absorption exist in the Near-Infrared range for vertical incidence of light for all samples. This can be observed in Fig. 4, where a plot with the results obtained from the simulation of vertical pillars of pitch 300 nm and radii 60 nm and of pitch 500 nm and radii 100 nm is shown. The wavelengths of these peaks are cross-listed in Table I. It can be noticed that the simulated peak positions for these two samples is almost the same. This fact can be explained because of the equal radius-over-pitch (r/a) value that these two structures have (0.2). Since the periodicity relationship observed by the electromagnetic waves is the same in both cases, their interaction with the systems would be expected to be similar.

However, one result of the simulation is that, as expected, the nanopillars height plays an important role in the final spectroscopic result. Fabricating nanopillars shorter than 2 μm causes the photonic crystal behaviour of the structure to become residual and no absorption bands can be seen in the simulation.

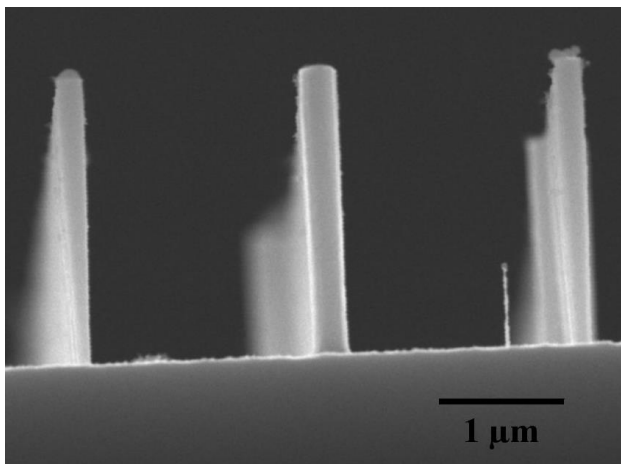


Fig. 5. SEM image of nanopillars of 100 nm radii where the negative tapering of the nanopillars can be observed.

IV. EXPERIMENTAL RESULTS AND DISCUSSION

A. Scanning Electron Microscopy (SEM)

Firstly, scanning electron microscopy (SEM) analysis is performed in order to determine the pillars' geometries and layout, their dimensions and to detect possible defects in the structures that may affect the result of the spectroscopic analysis.

The images that are shown in this section have been taken in a Jeol 7100 Field Emission Scanning Electron Microscope (FE-SEM) operating at 20 kV at CCIT of Universitat de Barcelona. In order to obtain top-view and cross-section morphological information of the fabricated nanopillars three different angle images (using different sample holders) have been employed: 0°, 45° and 90°.

These images have been useful for the improvement of the fabrication conditions and have been used to design new layouts in the different generation of samples. As can be observed in Fig. 5 the first nanopillars array showed non constant radius along the axial direction, some of them being strongly negatively tapered, which means that the radius at the bottom of the structures is smaller than at the top, result of the Bosch process. This result might be due to the difficulty of the flow of the protecting gas through high aspect ratio apertures, which results in low wall passivation the deeper the aperture is [6]. In Fig. 6 an extreme case of this negative tapering of the nanopillar is visible, where due to the charge accumulation during SEM inspection and the consequent apparition of electrostatic forces at the top of the nanopillars, they oscillate and touch one each other, remaining attached.

Fig. 7a shows a plan-view image of the nanopillar structure with gratings, described at the end of the fabrication section. And Fig. 7b and Fig.7c correspond to a detail of Fig. 7a of the grating area and part of the nanopillar arrays, respectively. In Fig. 8 the evolution and almost perfection of the nanopillars can be observed. However, 45 ° and 90 ° inclination images show several issues and non-desired defects in the fabricated nanopillars.

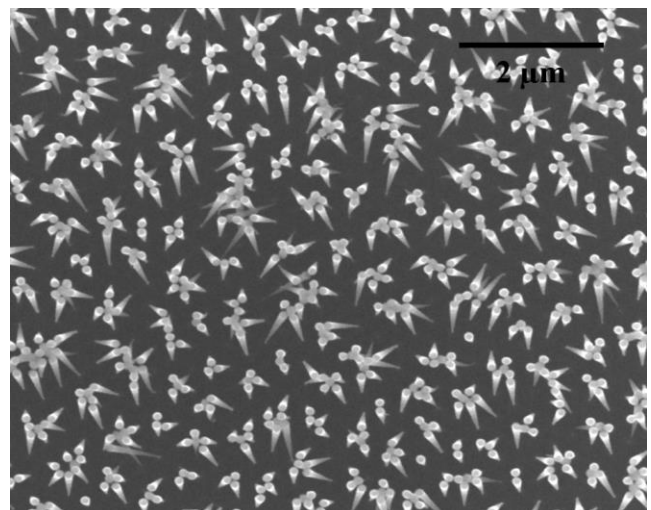


Fig. 6. Pillars bended due to the action of electrostatic forces during SEM inspection of a sample of 300 nm pitch and 60 nm radii.

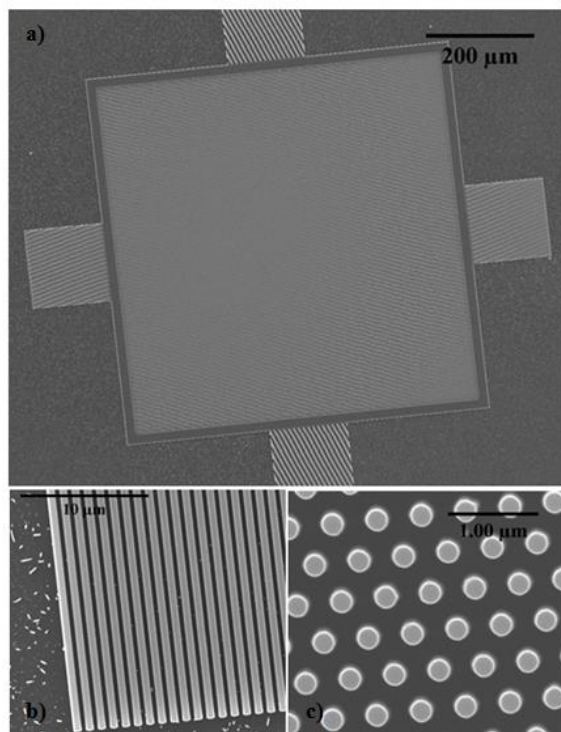


Fig. 7. Top view images taken during SEM inspection of a sample of pitch 500 nm and radii 100 nm. Showing (a) the system formed by nanopillars, gratings and walls; (b) detail of one of the gratings and (c) image of the nanopillar array.

One of the main concerns in the fabricated nanopillars, however, is still the fact that they do not have constant radius along the vertical direction. This can be clearly observed in Fig. 8, where the radius shrinks in the centre of the nanopillars (~190 nm) and increases again at the top and the bottom (~253 nm and ~245 nm, respectively). This phenomenon might have a different origin than that explained before. It can be caused due to the poor introduction of protecting gas in the gaps between the nanopillars during the pseudo-Bosch process. This effect is larger in samples with small pitch and/or increasing nanopillars' radii, because of the difficulty

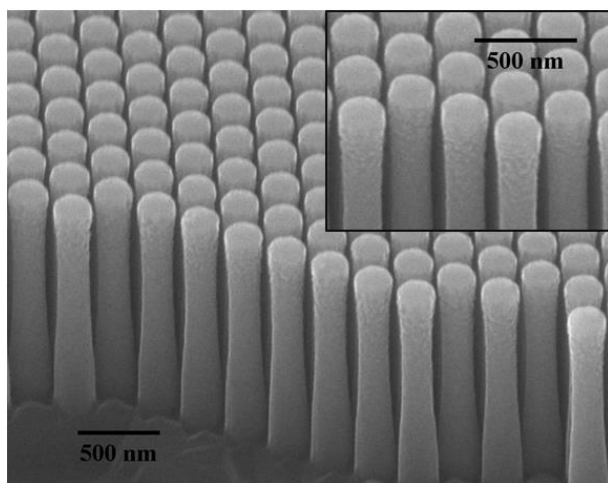


Fig. 8. 45° images taken from a broken sample of pitch 300 nm and radii 60 nm showing the final geometry of the nanopillars.

TABLE II
EXPERIMENTAL MEASUREMENTS OF NANOPILLARS DIMENSIONS

Parameter	500/100	300/100	300/60
Radius			
Top	109.0	126.7	58.0
Centre	-	95.0	-
Bottom	126.5	122.9	-
Height	1.9	-	-
Pitch	513.0	282.0	293.0

Experimental measurements of the nanopillars geometry from different samples, where the notation used for the samples name is pitch/radii, both in nm. Thus the nominal values of the radii and the pitch depend on the table column, and the nominal value of the height was 2 μm.

of the gases to reach the bottom of the attacked area.

Another effect that can be motivated by the fabrication process is the roughness on the upper part of the nanopillars. This phenomenon can be explained because of the condensation of the C_4F_8 on the nanopillars during the pseudo-Bosch process, forming small droplets on top of them and giving rise to the roughness observed.

Finally, in Fig. 9 an AFM ready sample image is shown. Again, the previously mentioned radius issue can be observed but, as was expected, less evident. However, another product of the fabrication process can be observed. Silicon vertical structures (so called nanograss) develop next to the pillars, sometimes with similar lengths. It is important to keep these random nanostructures in mind since they have a key role in the light interaction with our samples. Moreover, the observation of the samples lends us to think that an abundant and uncontrolled growth of this grass can end with the appearance of black silicon. Black silicon is based on a sort of silicon nano- and microstructures that suppress the reflexion and, thus, enhances the absorption of light and are a common product of Bosch and pseudo-Bosch processes [7]. The growth of these nanostructures on our samples may be taken under account since they can interfere in the final results obtained during the IR characterisation.

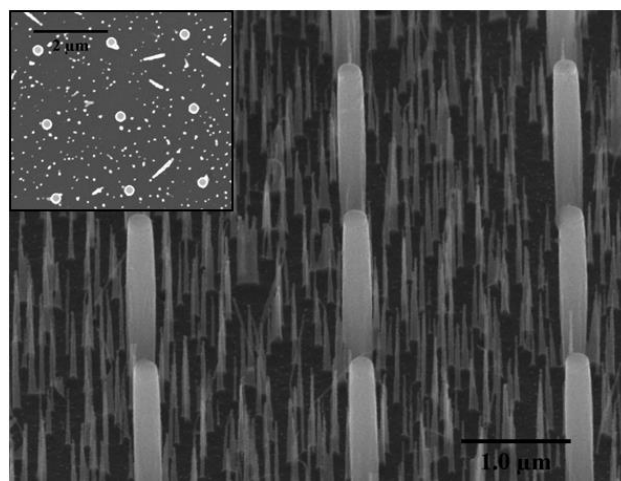


Fig. 9. 100 nm radius nanopillars where an improvement of the taper of the nanopillars can be observed in comparison to those shown in Fig. 5 The inset shows a top view of the nanopillars.

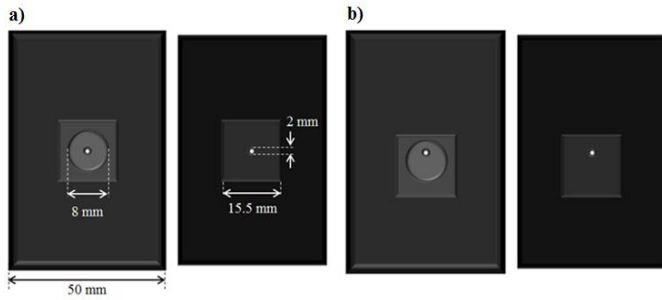


Fig. 10. Holders used during the IR characterisation of the samples. (a) The holder used for the photonic crystal characterisation and its measures and (b) the holder used for the background characterisation.

B. Infra-Red Spectroscopy (IR)

After the morphological analysis has been performed, spectroscopic measurements have been carried out. The system used is a FFT Perkin Elmer Frontier Infra-Red spectrometer (Fig. 8 shows the inside of the set up with the holder for normal incidence). This system performs the analysis in a wave number range between $8000 - 220 \text{ cm}^{-1}$ ($1.25 - 45.45 \text{ }\mu\text{m}$), which corresponds to the IR range of the electromagnetic spectrum. With a self-designed and self-constructed sample holder the correct alignment of the sample and the IR beam is achieved.

Two different holders have been used: one which allows the photonic crystal zone to be illuminated with the beam (Fig. 10a), and another where the substrate zone near the photonic crystal is illuminated (Fig. 10b).

The measurements have been taken with a total of 256 scans per spectra in order to maximize the signal-to-noise ratio. The signal is the percentage of transmitted light. Thus, further calculations must be performed in order to obtain the resulting absorbance curves. The acquisition process has been based on 3 different measurements: in air, on the background and on the photonic crystal.

The first one, in air, is needed in order to set the controlling software's zero and to ensure the constant behaviour of the source and the system during the samples analysis. This last verification is performed by taking the air signal several times between the samples' measurement and with the holder inside the system in order to compute the transmitted light through the diaphragm.

After this, a measurement of the silicon background is taken



Fig. 11. Set up used for IR analysis where the holder and the beam entrance and detection can be observed

in a region near the photonic crystal structure with the displaced holder and another at the photonic crystal with the centred holder. The former is needed in order to, during the further calculations, remove the substrate contribution and only analyse the photonic crystal's response. Moreover, since the fabrication process is not homogeneous over the wafer, the background signal must be taken near the photonic crystal in order to subtract the most accurate background for a specific measurement.

To perform the background subtraction and obtain the absorbance curves, one must take into account the relationship of intensities between the incident and the beam transmitted through the material:

$$I_{fin} = I_{ini} \cdot e^{-\alpha \cdot d} \quad (1)$$

Where, I_{fin} and I_{ini} are the transmitted and incident intensities, respectively, α is the absorption coefficient and d is the thickness of the sample. On the other hand, we can define the I_{fin} as the product of the intensities through the photonic crystal (I_{PC}) and the silicon substrate (I_{Si}):

$$I_{fin} = I_{Si} \cdot I_{PC} \quad (2)$$

To obtain the absorbance of the sample, the following expression, which uses equations (1) and (2), must be applied:

$$\alpha \cdot d = -\ln\left(\frac{I_{fin}}{I_{Si} \cdot I_{ini}}\right) \quad (3)$$

The samples that showed the best responses are those with a pitch of 500 nm and radii of 100 nm, and those with a pitch of 300 nm and radii of 60 and 100 nm. The results shown in this section correspond to the analysis of samples of the last two

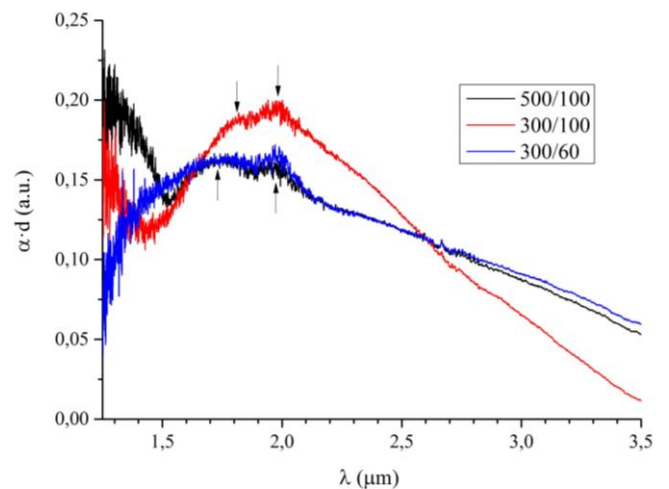


Fig. 12. IR results from the Generation #3 for the arrays with pitch of 500 nm and radii 100 nm (black), with pitch of 300 nm and radii 100 nm (red) and with pitch of 300 nm and radii 60 nm (blue). The arrows mark the peaks whose wavelength positions are listed in Table III.

TABLE III
EXPERIMENTAL MEASUREMENTS OF NANOPILLARS IR PEAKS

r (nm)	p (nm)	r/p	Peak 1 (μm)	Peak 2 (μm)
100	300	0.33	1.82	1.98
60	300	0.2	1.70	1.98
100	500	0.2	1.75	1.95

Results obtained from Generation #3, where the nanopillars' nominal height is $2 \mu\text{m}$ and one single background used for measurements.

generations. The only difference between them is the nanopillars height; Generation #3 has a nominal value of $2 \mu\text{m}$ and Generation #4, of $3 \mu\text{m}$. In addition, the background signal used in Generation #3 was taken only once at the edge of the wafer and it was considered to be the same for all the structures. On the other hand, the background used for the data treatment in Generation #4 was taken near each photonic crystal structure.

The results summarized in tables III and IV show the analysis of the peaks observed in Figs. 12 and 13. Several tendencies can be observed.

First of all it must be pointed out that, as simulations show, the response for nanopillars with a height of $2 \mu\text{m}$ is smaller than those of $3 \mu\text{m}$. This fact can be directly correlated to the total amount of material that behaves as photonic crystal (scattering volume). If the nanopillars are higher, the volume that interacts with light is larger and the response, too. In the same direction, this idea can be also applied to the differences between the larger and smaller values of the absorption spectra of different structures from Generation #4. Those samples with higher density of nanopillars present higher values of absorbance due to a larger volume of interaction with the electromagnetic waves.

On the other hand, the tendency predicted in simulations, that those samples with the same radius-to-pitch relation

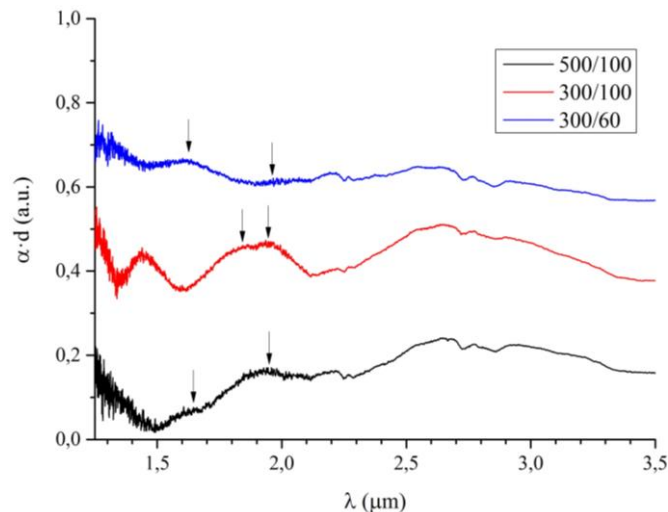


Fig. 13. IR results from the Generation #4 for the arrays with pitch of 500 nm and radii 100 nm (black), with pitch of 300 nm and radii 100 nm (red) and with pitch of 300 nm and radii 60 nm (blue). The arrows mark the peaks whose wavelength positions are listed in Table IV.

TABLE IV
EXPERIMENTAL MEASUREMENTS OF NANOPILLARS IR PEAKS

r (nm)	p (nm)	r/p	Peak 1 (μm)	Peak 2 (μm)
100	300	0.33	1.85	1.93
60	300	0.2	1.62	1.94
100	500	0.2	1.62	1.92

Results obtained from Generation #4 for nanopillars nominal height of $3 \mu\text{m}$ and different background taken near each photonic crystal structure.

behave similarly, is also verified and clearly observed in Fig. 12, where it is evident that the absorbance spectra of samples 500/100 and 300/60 almost overlap. Data shown in tables III and IV also confirm this statement.

In addition, it is observed that the larger the radius-to-pitch relationship, the more the peaks displace towards larger lambda values, valid for equivalent peaks. However, the measured peak positions do not perfectly match those predicted by simulations. This fact can be explained because of to the non-cylindrical shape of the pillars, despite the fact that the fabrication process has improved reasonably among samples' generations. Since the simulations carried out are performed under ideal cylindrical structures, we would expect a non-perfect match between the experimental and simulated peaks. However, the differences are small and this result is encouraging.

Another feature worth mentioning is a peak appearing in all the samples at the same position of $1.95 \mu\text{m} \pm 0.3 \mu\text{m}$. Its origin can be explained keeping in mind the grass developed in some RIE processes at the surface, which is known as black silicon for very high "grass". It is found in literature [8] that the absorbance spectrum of "black silicon" has a pronounced peak at wavelengths around $2 \mu\text{m}$. Even the samples which have given rise to the best nanopillars still show the presence of grass. This effect is much less pronounced for the samples of Generation #3 where the background was taken at the edge of the wafer, where the grass density is lower.

V. CONCLUSIONS AND FURTHER WORK

In this work the first experimental implementation and characterisations of silicon nanopillars arrays in hexagonal lattices with the purpose to measure their properties as photonic crystals have been presented. Up to four different generations of samples have been fabricated with the aim of improving final geometry and layout of the structures, which has been tuned by simulations. From these, the theoretical responses of the nanopillar arrays have been extracted, showing two absorption peaks in the NIR wavelength region, which is the desired one. In addition, they predicted that the correlation radius-to-pitch plays an important role on the wavelength of the mentioned peaks.

Morphological analysis, performed by SEM, confirms the relation between the nanopillar shape and the used process and has allowed optimising the latter. Furthermore, these geometrical features have been used to understand the FTIR measurements.

FTIR results confirm the presence of absorption peaks related to the geometry of the array and that are in good agreement with the simulations. The small discrepancies shift towards larger wavelengths, can be understood based on the fabricated geometrical parameters. In addition, an absorption band around 2 μm , which does not overlap with the searched absorption peaks of the photonic crystal, appears in all the samples and can be attributed to the presence of nanograss, an unwanted result of the reactive ion etching fabrication process.

As this is a long lasting project, further works are to be performed. The initial phases of this work are indicated in the following:

First, the optimisation of the fabrication routes towards an even better nanopyllar array, even though the structure is already quite good. Secondly, the FTIR measurements in water environment, as this will be the real conditions for which the devices are designed. As a third point, the deflection of the nanopyllars to obtain a force-deflection curve and the simulation of this effect on the optical bandgap structure.

ACKNOWLEDGMENT

First of all, I would like to acknowledge my thesis professor Albert Romano for his patience and his valuable advice and guidance during these months. I would like to acknowledge too Professor Mauricio Moreno and the IR technician Dr. Núria Ferrer for their supporting counsel.

I would like to acknowledge too my companion, Alejandro Hernández, my parents and my master colleagues, my teammates and my friends for their support and patience during the development of this work.

REFERENCES

- [1] J. D. Joannopoulos, S. G. Johnson, J. N. Winn and R. D. Meade (2017, November, 13). *Photonic Crystals: Molding the Flow of Light* (2nd Edition). Available: <http://www.ab-initio.mit.edu/book/photonic-crystals-book.pdf>
- [2] I. Rodríguez García, "Nanopyllar structures for stress measurements in biological tissues", unpublished.
- [3] J. Esteve Sorribas (2016, January). Study of 2-D Photonic Band Gaps for NIR applications. Available: <http://hdl.handle.net/2445/96314>
- [4] A. A. Tseng, K. Chen, C. D. Chen and K. J. Ma, "Electron Beam Lithography in Nanoscale Fabrication: Recent Development," *IEEE Trans. Electronics Packaging Manufacturing*, vol. 26 (2), pp. 141-149, Apr. 2003.
- [5] F. Laermer, A. Schilp, K. Funk, M. Offenberger and R. Bosch, "Bosch deep silicon etching: improving uniformity and etch rate for advanced mems applications," *in 1999 IEEE*, pp. 211-216.
- [6] S. S. Walavalkar, A. P. Homyk, M. D. Henry and A. Scherer, "Three-dimensional etching of silicon for the fabrication of low-dimensional suspended devices," *Nanoscale*, vol.5, pp. 927 -931, 2013.
- [7] X. Liu, P. R. Coxon, M. Peters, B. Hoex, J. M. Cole and D. J. Fray, "Black silicon: fabrication methods, properties and solar energy applications," *Energy Environ. Sci.*, vol. 7, pp. 3223-3263, 2014.
- [8] C. Wu, C. H. Crouch, L. Zhao, J. E. Carey, R. Younkin, J. A. Levinson, E. Mazur, R. M. Farrell, P. Gothoskar and A. Karger, "Near-unity below-band-gap absorption by microstructured silicon," *Appl. Phys. Lett.*, vol. 78 (13), pp. 1850-1852, 2001.